Circulation Control of a Channel Wing using Discrete Coanda Actuation

Bojan Vukasinovic [1], Robert B. Funk [2], Carl Johnson[3], and Ari Glezer[4]

[1,4]Woodruff School of Mechanical Engineering,
Georgia Institute of Technology, Atlanta, GA 30332-0405

[2]Georgia Tech Research Institute ATAS, Smyrna, GA 30080

[3] School of Aerospace Engineering,
Georgia Institute of Technology, Atlanta, GA 30332-0405

Abstract

Aerodynamic flow control of a channel wing model using fluidic actuation was investigated in wind tunnel experiments. Trailing edge circulation control (CC) for enhancement of short takeoff and landing (STOL) was effected using independent arrays of fluidically oscillating jet actuators integrated with Coanda surfaces upstream of a 45° flap of the wing's outboard segment and along the trailing edge of the channel. In addition, the effectiveness of CC was extended into the stall regime by arrays of fluidically oscillating jets along the wing leading edge. The utility of fluidic actuation for CC was assessed in the absence and presence of power to the channel propeller drive over a range of thrust coefficients $0 < C_T < 1$. The present investigations demonstrated that lift enhancements by CC control on the outboard wing segment and on the channel are additive and therefore the actuation can be distributed in different proportions to achieve an overall desired lift increment. It was also shown that in the absence of power to the channel propeller, CC control can lead to a nearly invariant lift increment at $0° < \alpha < 10°$ where the lift increment effected on the channel is at least $\Delta C_L = 1.5$. In addition, augmentation by the powered propeller yields an increment of at least $\Delta C_L = 2$. Peak effectiveness was attained at $\alpha = 4°$ at which $\Delta C_L = 2.3$ and 2.5 for $C_T = 0.6$ and 1, respectively. System level assessment of a hybrid electric STOL transport UAV based on the channel wing data showed that trailing edge CC can enable up to 73% reduction in liftoff distance.

I. Background

Slotted airfoils, both open and pressurized, have been employed in the field of high-lift aerodynamics as far back as in the 1930s and even earlier, as summarized by Haus (1931), including a 2-D jet issuing tangent to a flap having a sharp trailing edge. A review of high-lift applications in the 1950s by Williams, et al. (1961) noted an extension of trailing edge high-lift control to jet flaps or blown flaps in which a 2-D jet issued at a fixed angle from the trailing edge of the airfoil (e.g., Davidson 1956 and Dimmock 1957). This 2-D jet augmented the aerodynamic forces by pneumatically entraining and deflecting the flow over the airfoil effectively acting as an

[1] Research Engineer, AIAA Member.
[2] Research Engineer, AIAA Associate Fellow.
[3] Research Engineer, AIAA Member.
[4] Professor, AIAA Fellow.

extended camber. This approach that was thought of as a 'pneumatic flap' was shown to be effective when sufficient compressed air was available on-board. The aerodynamic actuation concept that has come to be known as Circulation Control (CC) is follow-on to the jet flap with a in which significant performance improvement was realized by replacing the flap with a convex trailing edge surface and exploiting the Coanda effect of the attached tangential 2-D jet by balancing the centrifugal force with the suction pressure over the surface.

In addition to trailing edge circulation control concepts, another unique high-lift concept was proposed by Custer (1929) in which the wing was modified to incorporate a channel section near its root that encloses the lower half of the propeller arc. The lift induced by the propeller-generated flow over the channel's inner surface combined with the thrust at nonzero angles of attack enables the aircraft to take off and sustain flight thereafter at low takeoff speeds and short distances. This concept engendered significant initial interest culminating in a full-scale test (Pasamanick, 1953). Further analysis was later provided by Blick and Homer (1971). Although the channel wing was successfully demonstrated on several generations of airplanes over subsequent decades, up-and-away performance and the engine-out occurrences resulted in virtually no commercial adoption (Gunther et al. 2000). However, recent increasing demand for short take-off and landing (STOL) concepts has triggered renewed interest in channel wings that has been, primarily fuelled by rapid expansion of unmanned aerial vehicles (UAVs) and urban mobility needs (e.g., Keane and Keane, 2016, Mihalik and Keane, 2022). In addition to the use of the powered flow over the wing channel, the wind tunnel investigations of Englar and Campbell (2002) augmented the high lift capabilities of a powered channel wing model by implementing circulation control (CC) based on the Coanda effect of a steady, nominally 2-D jet over the channel's rounded trailing edge and reported lift enhancement up to $C_L = 9$, albeit at significant actuation momentum coefficients.

The present experimental investigation builds on the earlier investigations of Vukasinovic et al. (2023a, b) and focuses on the use of circulation control for enhancing the STOL and manoeuvring characteristics of a powered channel wing by using fluidic actuation along the channel's trailing edge and over the flap on the outboard section of a channel wing. Unsteady Coanda-assisted circulation control is effected using 3-D by arrays of discrete fluidically oscillating wall jets integrated into rounded Coanda surfaces. The present data was integrated in a system level assessment model of a hybrid electric STOL transport UAV to assess potential reductions in liftoff distance.

II. Experimental Setup and Procedures

The investigations were conducted in the Harper 7 × 9 ft. (2.1 × 2.7 m) Wind Tunnel, a closed circuit, single return, atmospheric wind tunnel at the School of Aerospace Engineering at Georgia Tech. The facility is driven by a 600 horsepower (447 kW) electric motor, controlled with a variable frequency drive providing continuous speed control, and coupled to a four bladed, fixed pitch fan. The speed in the test section can be continuously varied up to 165 ft/s (50 m/s) and is measured using a Pitot-static probe. Turbulence in the test section (0.3%) is minimized by use of honeycomb and fine mesh screens. A breather downstream of the test section maintains the test section at atmospheric pressure.

Figure 1a shows an upstream view of the channel wing model installed in the wind tunnel test section on a rotational stage that protrudes through an elevated ground plane above the test section floor to reduce the effects of the wall boundary layer. The channel wing model was built on a

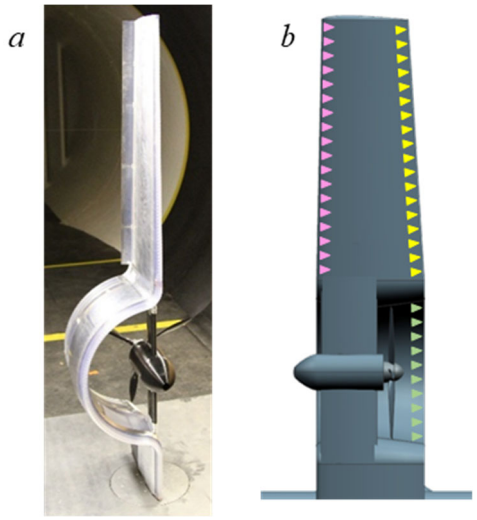

Figure 1. *The channel wing model installed in the wind tunnel (a) and a planform CAD illustration showing the motor and the arrays of the fluidically oscillating jet actuators along the trailing edges of the wing's* ***outboard segment****,* ***channel****, and* ***leading edge.***

ladder frame consisting of two spars held together with chordwise spacers and is based on an NACA 64A214 airfoil, has a span of 1.68 m and a 0.51 m diameter channel within from $0.149 < z/s < 0.45$ (z is measured from the root). The outboard section of the wing (0.924 m span) is tapered (leading/trailing edges 1.16°/-3.53°) such that the chords at the channel and the tip are 0.354 m and 0.283 m, respectively, yielding $\bar{c} = 0.318$ m. The aerodynamic loads on the model are measured using a combination of a 6-DOF force sensor and two single axis load cells added to absorb forces due to rolling moments beyond the range of the 6-DOF sensor. The model includes three arrays of fluidically oscillating jet actuators that are integrated with modular pneumatic plumbing and fabricated using SLA. The three fluidic flow control arrays are shown schematically in Figure 1b and are color coded as delineated in Figure 1b, where the trailing edge wing and channel arrays are color coded in red and teal, respectively, while the wing leading edge array is represented in purple, and were individually controlled by manually operated external pressure regulators. The pressure in each supply plenum was monitored, and the flow rate to each fluidic array was measured with either a venturi flowmeter or a critical flow nozzle. The leading-edge flow control array was intended to be used only past the incipient stall and was only tested under such specific conditions, in addition to the wing trailing edge fluidic flow control.

The propulsion flow through the channel is driven by a three-bladed propeller attached to an electric motor (Hacker Q80) mounted on the model as shown in Figure 1a and controlled from the laboratory computer using speed controller (*Jeti Masterspin Pro* 220). The propulsion thrust was characterized on a separate vertical test stand in the wind tunnel over a range of tunnel speeds (up to 24 m/sec) and motor RPM (the drag of the test stand and nacelle were measured in the absence of the propeller to correct the measured thrust). The propeller was characterized at its final trimmed size (0.50 m diameter) required to fit in the channel (original size 20×14, 20" diameter, 14" pitch). The thrust and torque coefficients C_T and C_Q were computed based on the tunnel speed and the advance ratio (Ψ = tunnel speed/tip speed) as shown in Figure 2. The advance ratio was used with a

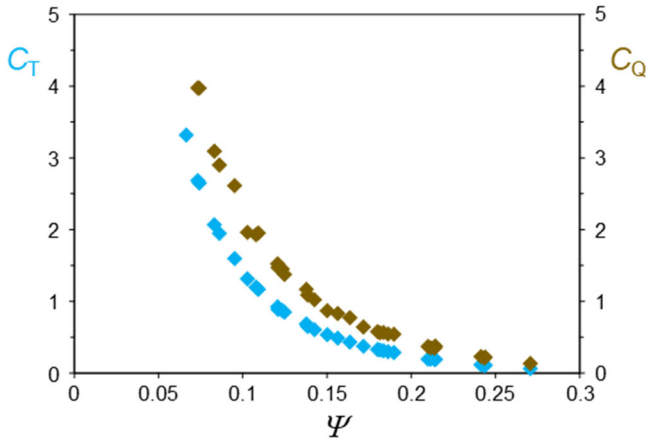

Figure 2. *Variation of the* ***thrust*** *and* ***torque*** *coefficients* C_T *and* C_Q *with advance ratio □ of the isolated propeller.*

calibration equation developed from the isolated testing to calculate C_T during the channel wing testing.

For the purpose of the current work, the trailing edge of the channel wing model was modified relative to the earlier study of Vukasinovic et al. (2023b), while fluidic actuation was still integrated within two self-contained arrays along and upstream of the trailing edge flap of the outboard wing segment and along the channel's trailing edge, two changes were made in the current model to improve CC effectiveness near the wing tip by reducing the 0.1c flap deflection angle to $\phi = 45°$from the aggressive 70º in the earlier model, and by improving the integrated Coanda surface leading to the flap. In the present study the normalized radius of the Coanda surface r/c was spanwise invariant ($r/c = 0.06$) and therefore r varied monotonically with the tapering of the wing. Also, unlike the bi-directional fluidic actuation at the trailing edge of the channel in the earlier study, circulation control at the trailing edge of the current channel section is one-directional and coupled to a quarter-round Coanda surface. As in the earlier model, an independent array of fluidic oscillators is used along the outboard segment of the wing's leading edge to enable circulation control at the trailing edge during incipient stall. The independent actuation configurations along the trailing edges of the wing's outboard section and of the channel are referred to as WTE and CTE, respectively, and the configuration along the outboard segment of the wing's leading edge is referred to as WLE. The three actuator arrays can be activated individually or in any combination when the propeller is stationary or powered and the data presented in §§ IV and V are color coded accordingly. The present investigations were conducted over a range of tunnel speeds up to $U_o = 24$ m/sec ($q = 7$ psf), and $Re_c = 536{,}700$.

Similar to the earlier investigations of CC over a 2-D airfoil (Vukasinovic et al., 2023a), the actuation is characterized using the actuation mass flow rate and momentum coefficients, $C_q = \dot{m}_{jet}/(\rho_o \cdot U_o \cdot A_p)$ and $C_\mu^F = T/(q \cdot A_p)$, respectively where T is the total force effected by the actuation jets in the absence of cross flow (quiescent conditions). For a given mass flow rate as measured by the mass flow coefficient C_q, C_μ^F measures the magnitude of the resultant aerodynamic load that is effected by a specific configuration of integrated fluidic actuators on the aerodynamic platform in the absence of crossflow. This aerodynamic force coefficient C_μ^F is related to the conventional momentum coefficient $C_\mu = J/(q \cdot A_p)$ that is based on the magnitude of the momentum flux J of the fluidic actuation jets (essentially the total thrust of the actuation). Because it is usually difficult to measure the cumulative C_μ of multiple actuation jets directly, the velocity distributions across multiple the orifices of the actuation jets are typically not fully characterized. These difficulties can be overcome by characterizing the actuation using C_μ^F that can be measured simply and directly *in situ* by using the system's balance or load cells.

III. Characterization of the Actuation Jets and Propeller-Powered Channel

Following the discussion in §II, and similar to the calibration procedure of the actuation modules outlined by Vukasinovic et al. (2023b), the wing's outboard and channel trailing edge actuators as well as its leading-edge actuators were calibrated in the absence of cross flow by measuring the variation of the aerodynamic load $\vec{T}$ effected by the actuation jets with the actuation mass flow rate. Sectional tufts visualization of the control jet flow over the flap was conducted to verify jet attachment along the flap (the Coanda surface at the jet exit plane terminates at the flap). A sample of the tufts flow visualization in Figure 3a shows that in the presence of active jets the tufts distributed along the downstream section of the flap ($\phi = 45°$) remain attached to the surface. The

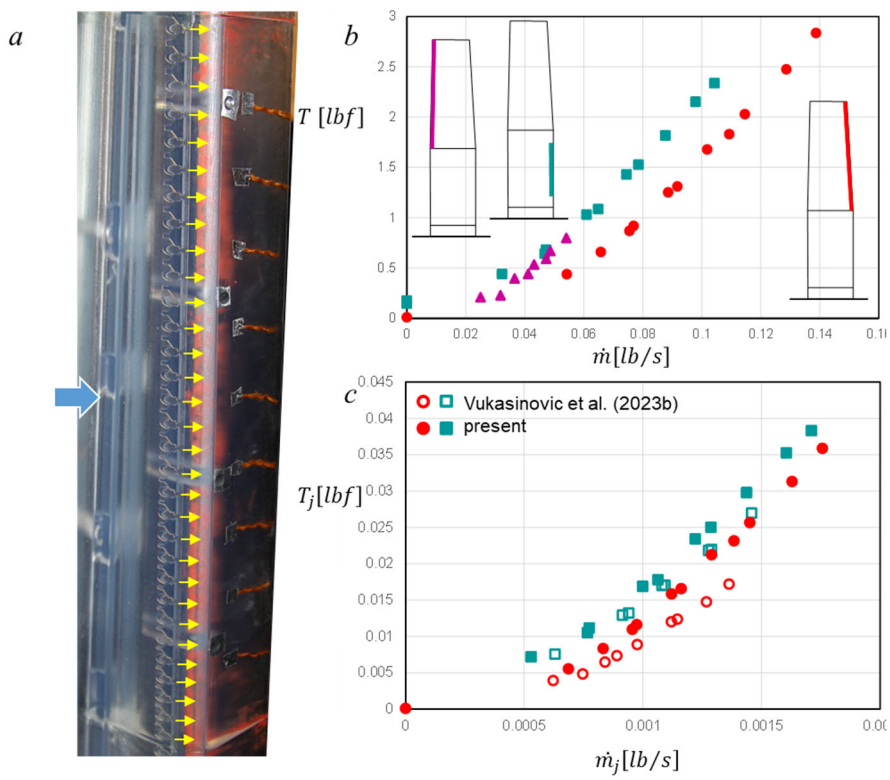

Figure 3. *a) Sectional tuft visualization of the trailing edge jets in the absence of crossflow; b) In situ variation with actuation mass flow rate $\dot{m}$ of the actuation load T effected by the fluidically oscillating actuator arrays along the trailing edges of the wing's* ***outboard*** *and* ***channel*** *segments (configurations WTE and CTE), and the wing's* ***leading edge*** *(WLE) where the active actuation arrays are shown schematically in the insets; and c) Variation of the actuation load with mass flow rate per (single) actuator T_j and $\dot{m}_j$, respectively. The corresponding data of Vukasinovic et al. (2023b) is included in (c) for reference (open symbols).*

variation of the magnitude of the load effected by the jet array T with actuation mass flow rate shown in Figure 3b indicates quadratic dependence as shown by Vukasinovic et al., 2023b). These data show that the outboard jet array over the flap (configuration WTE) effects a lower force that may be attributed to the differences in the Coanda surfaces between the channel (cylindrical) and outboard segment (flap). However, considering the difference in the number of actuators, it is noted that the disparity in load per actuation jet is notably lower when compared based on the mass flow rate per jet as shown in Figure 3c. These data show that the actuation jets at the trailing edge of the channel (configuration CTE) that are integrated with a cylindrical Coanda surface outperform only slightly the outboard jet actuators that are integrated with a flap. Furthermore, the integration of the actuators to the trailing edges of the channel and the flap was significantly improved compared to the investigations of Vukasinovic et al. (2023b).

The effects of the trailing edge actuation on takeoff at zero ground roll (or vertical takeoff capabilities) were investigated in the absence of a cross flow using the channel's trailing edge actuation (CTE) in the presence of channel flow induced by the powered propeller in terms of the effected lift and drag. These tests were conducted at $\alpha = 0$ (to avoid interference with the test section sidewalls) at three propeller angular speeds $\Omega = 3{,}000$, 5,000, and 6,000 RPM (corresponding to $C_T = 0.138$, 0.612, 0.927 at $U_o = 18.2$ m/sec). The resulting (dimensional) lift is shown in Figure 4a. When the propeller is powered in the absence of actuation, the flow within the channel induces net lift of up to $L = 10$ lbf at 6,000 RPM. As the actuation mass flow rate $\dot{m}$ is increased, vectoring of the channel flow about the trailing edge Coanda surface increases the effected lift exceeds by over two-fold at $\dot{m} = 0.1$ lb/sec. The resulting horizontal negative force (colinear with the actuation's lift induced drag) in Figure 4b indicates the thrust generated by the

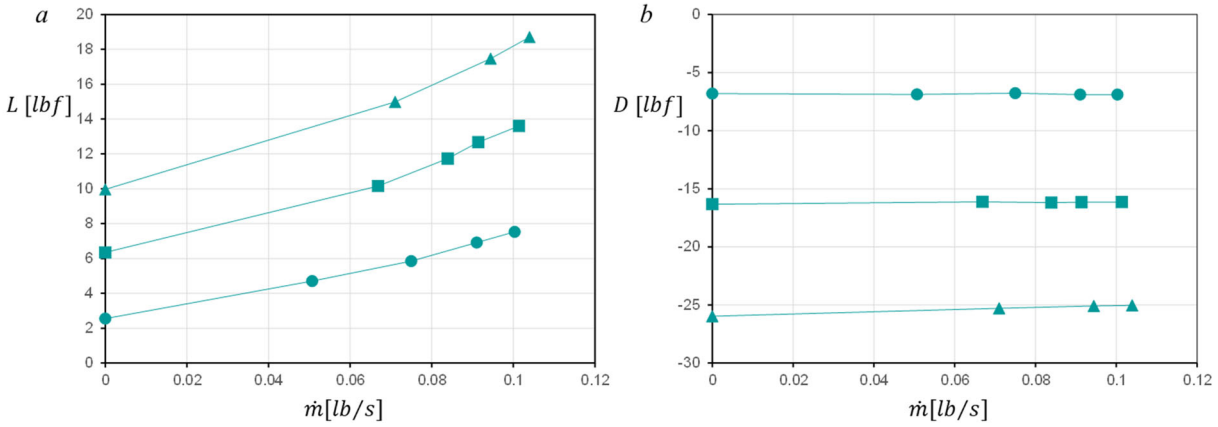

Figure 4. *Variation of the lift (a) and drag (b) with actuation mass flow rate at the channel's trailing edge (CTE) effected by the powered propeller on the channel wing $\alpha = 0°$ in the absence of a cross flow at $\Omega = 3{,}000$ (●), 5,000 (■), and 6,000 (▲) RPM (or, for reference, $C_T = 0.138, 0.612, 0.927$ at $U_o = 18.2$ m/sec).*

propeller with increasing RPM. In the presence of actuation, the thrust effected by the propeller decreases slightly with increasing $\dot{m}$ as the lift vector tilts in the streamwise direction. These data show that in principle, it should be possible to generate higher lift in the absence of cross flow when the channel wing is oriented at a $\alpha > 0$ where a fraction of the generated thrust shown in Figure 4b would also contribute to lift.

IV. Circulation Control

The aerodynamic characteristics of the baseline channel wing and in the presence of circulation control were first characterized in the absence of propeller power ($C_T = 0$, but with propeller installed). The variation of the lift and drag coefficients with angle of attack for the baseline model at $U_o = 18.2$ m/sec ($q = 4$ psf) are shown in Figure 5 for flap deflections of $\phi = 45°$ (current model, the present CC investigations are primarily focused on the range $0 < \alpha < 10°$) and 70° (Vukasinovic et al., 2023b). These data show that below stall ($\alpha \approx 9°$) the lift and drag do not vary appreciably with ϕ and the C_L is nearly linear with α ($dC_L/d\alpha \approx 0.07$). For $\phi = 70°$ the onset of stall occurs at $\alpha \approx 8°$ ($C_L \approx 1.2$), while for $\phi = 45°$ $C_L \approx 1.3$ at $\alpha \approx 10°$. The drag increases nearly monotonically although the rate of increase at $\phi = 45°$ is somewhat lower, and at $\alpha = 9°$, $L/D = 6.5$.

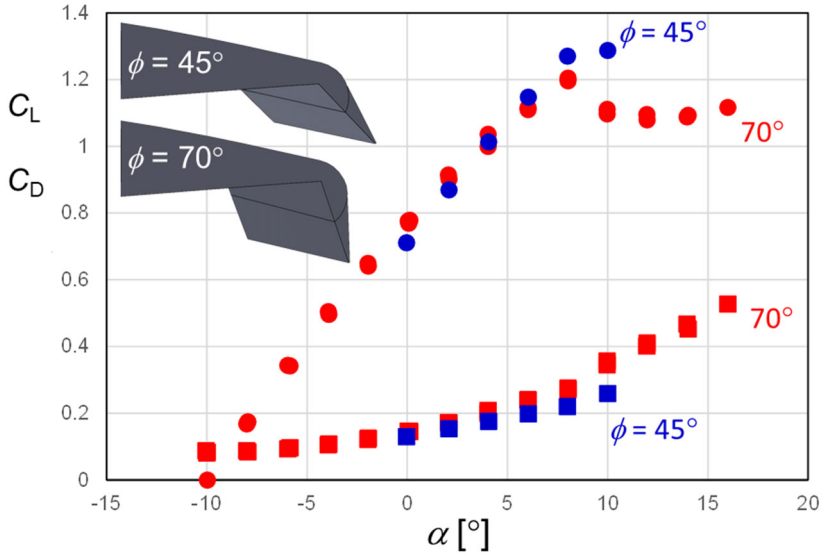

Figure 5. *Variation of the lift (●) and drag (■) of the baseline channel wing with angle of attack at flap angles $\phi = 45°$ and 70° (Vukasinovic et al., 2023b).*

Tufts visualization over the trailing edge/flap on the outboard segment of the wing (Figure 6a) at $\alpha = 6°$ and $U_o = 18.2$ m/sec ($q = 4$ psf) show that in the absence of actuation the flow over the flap ($\phi = 45°$) is stalled (Figure 6b) indicating that the flow has a significant outboard velocity component across the flap. However, once actuation is effected along the trailing edge upstream of the flap juncture (e.g., at $C_\mu^F = 0.04$), the flow over the flap becomes fully attached and appears to be mostly streamwise as is illustrated in Figure 6c. The variation of the lift and drag increments effected by trailing edge actuation along the outboard section of the wing at $\alpha = 6°$ with the momentum coefficients C_μ^F at are shown in Figures 7a and b, respectively. It is noteworthy that the lift and corresponding lift induced drag increments are nearly invariant at $U_o = 18.2$ and 23 m/sec ($q = 4$, and 6 psf) where full attachment as indicated by tufts visualizations occurred at $C_\mu^F = 0.038$, respectively. However, at a lower speed $U_o = 12.9$ m/sec ($q = 2$ psf), the corresponding lift and induced drag increments are somewhat lower (e.g., by nearly 10 and 30%, respectively at $C_\mu^F = 0.047$, full tufts attachment occurred at $C_\mu^F = 0.047$ indicating that at lower speed the turning of the cross flow yields lower increases in circulation. Furthermore, it is noted that at $U_o = 18.2$ and 23 m/sec ($q = 4$, and 6 psf), ΔC_L exhibits a nearly-linear variation with C_μ^F in two distinct rates below and above $C_\mu^F \approx 0.03$. This change in the rate of variation of ΔC_L with C_μ^F was observed by a number of earlier investigators (e.g., Jones, 2005, Radespiel et al., 2016) who argued that it results from transition from "boundary layer (or separation) control" to "circulation control" in which the rate of increase in lift with C_μ^F that is associated with the turning of the cross flow diminishes (of course, in either regime the change in induced lift is associated with a change in circulation). However, at $q = 2$

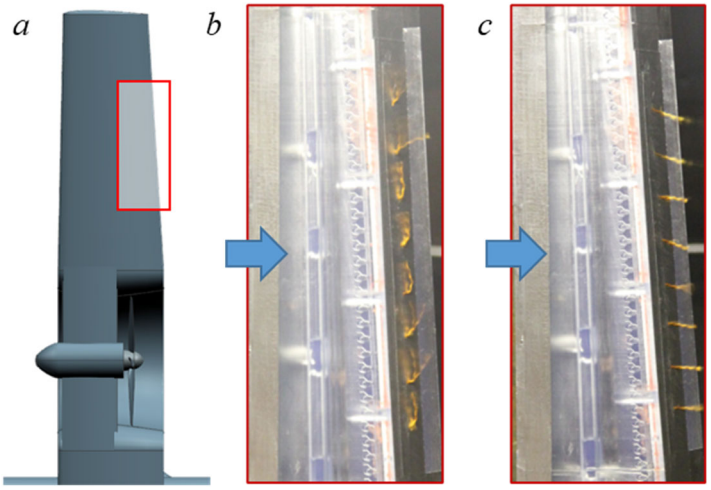

Figure 6. *Sectional tufts visualization along the trailing edge segment shown in (a) in the absence (b) and presence (c) of trailing edge actuation: U_o=18.2 m/sec, $\alpha = 6°$, $C_\mu^F = 0.04$.*

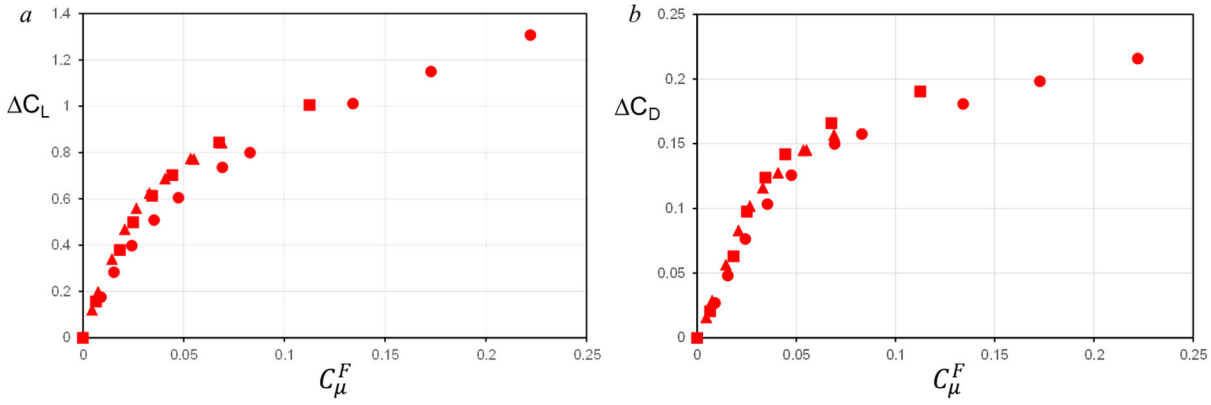

Figure 7. *Variation of the lift (a) and drag (b) increments effected by trailing edge actuation along the outboard section of the wing with C_μ^F at U_o = 12.9 (●), 18.2 (■) and 23 (▲) m/sec (q = 2, 4, and 6.4 psf) and $\alpha = 6°$.*

psf, ΔC_L does not increase linearly with C_μ^F below 0.05 but does so above it at nearly the same rate as at at the higher speeds for $C_\mu^F > 0.03$ exhibiting a different upper limit in the "separation control" regime while the increase in circulation that is manifested primarily by turning of the outer flow occurs at the same rate at the three cross flow speeds. As noted above, the corresponding changes in the lift induced drag increments in Figure 7b closely follow the pattern of the lift increments.

The lift and drag increments relative to the baseline effected by the actuation at seven equally-incremented cross flow dynamic pressures ($9.1 < U_o < 24.1$ m/sec, $1 < q < 7$ psf) in the absence and presence of powered propeller are summarized in Figures 8 and 9, respectively (in the data sequence of each actuation configuration q increases from left to right). As expected, as the cross flow speed decreases the effected lift increments ΔC_L increase with C_μ^F (Figure 8a) at each of the three actuation configurations (WTE, CTE, and C/WTE). While at a given C_μ^F, WTE actuation effects a higher increase in lift than the CTE, the higher performance is associated with the larger fraction of the model's trailing edge occupied by the WTE actuator array comparted to the CTE array. Perhaps more importantly, when the effects of the two actuation configurations are considered separately at, say, $C_\mu^F = 0.21$ and 0.16, respectively (marked by teal and red arrows) and then are combined at the sum $C_\mu^F = 0.37$ (marked by stacked arrows), their effects are *additive*, implying a simple superposition of their individual effects in the absence of interference between them. For reference, the figure also shows the lift increments effected by each of the three actuation configurations at a given cross flow speed (q = 1, 2, and 7 psf or U_o = 9.1, 12.9, and 24.1 m/sec) using dashed lines. These data show that in the absence of propeller power C/WTE actuation can yield ΔC_L as high as 1.25, 2, and 2.9 at q = 7, 2, and 1 psf, respectively. The corresponding actuation effects in the presence of the powered propeller are shown in Figure 8b. In the absence of actuation, the powered propeller at constant RPM (0.59 (q=7 psf) < C_T < 4.26 (q=1 psf)) increases ΔC_L from about 0.5 to about 2 as q is decreased from 7 to 1 psf (from 24.1 to

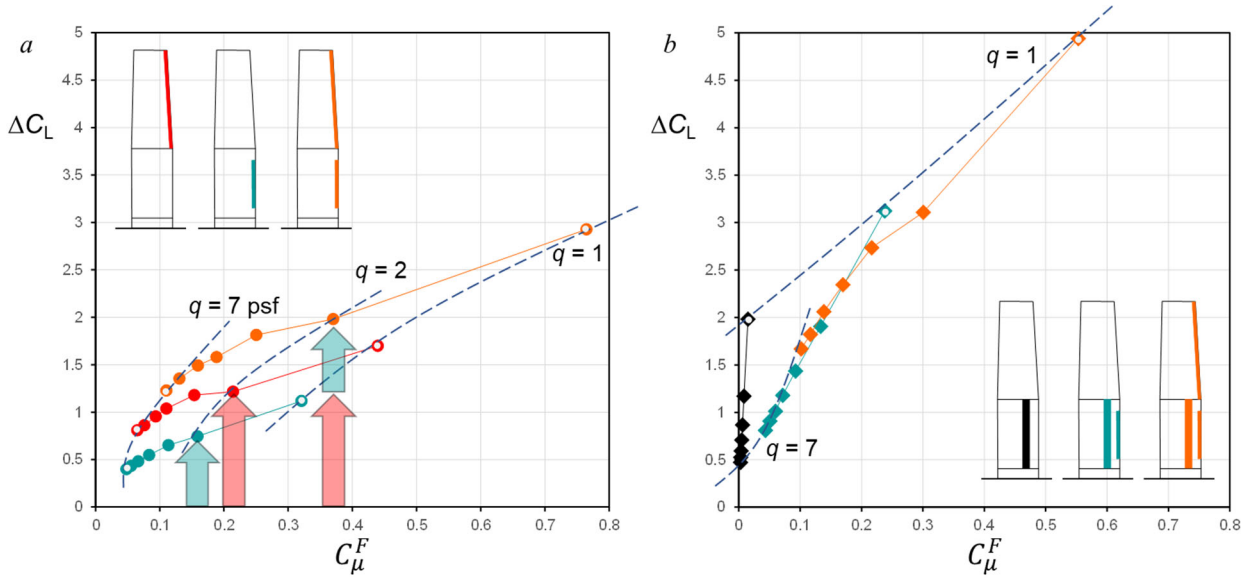

Figure 8. *The lift increments relative to the baseline effected by actuation at seven equally-incremented cross flow dynamic pressures (9.1 < Uo < 24.1 m/sec, 1 < q < 7 psf, α = 6°) in the absence and presence of powered propeller. In the data sequence of each actuation, q increases from right to left. For reference, the lift increments effected by each of the configurations WTE, CTE, and C/WTE at q = 1, 2, and 7 psf (Uo = 9.1, 12.9, and 24.1 m/sec) are marked using dashed lines through open symbols.*

9.1 m/sec). The addition of fluidic actuation at the trailing edge of the channel leads to increased ΔC_L with C_μ^F at each C_T up to $\Delta C_L = 3.2$ from 2 at the highest C_T (4.26). *The addition of WTE shows a significant range of the total C_μ^F at which significant increases in ΔC_L can be attained by combinations of WTE and CTE actuation up to $\Delta C_L \approx 5$ (from $\Delta C_L = 2$ in the absence of actuation) at $q = 1$ psf and $C_\mu^F = 0.56$ indicating the potential utility for enabling short takeoff and landing.*

Similar to Figure 8, the corresponding effects of the three actuation configurations on the lift-induced drag increments are assessed in Figures 9a and b in the absence and presence of propeller power, respectively. As shown in Figure 9a CTE actuation leads to a small lift-induced drag with small variations with free stream speed. This finding is in accord with the earlier investigations of 2-D wing configurations of Vukasinovic et al. (2023a), where it was shown that compared to 2-D actuation, 3-D segmented actuation leads to higher lift and lower lift-induced drag that can be attributed to the higher Coanda jet force of the 3-D actuators that result in shallower streamwise deflection of the effected Coanda lift force. The induced lift induced drag increases with WTE actuation as a result of the deflected flap and it is also dominant when both CTE and WTE actuation is used. In the presence of propeller power (Figure 9b), the reduction in drag decreases with increasing cross flow speed (from -3 to -0.5 with q = 1 to 7). The incremental increases in ΔC_D by the lift induced drag of CTE actuation are larger than when $C_T = 0$ owing to the streamwise tilting of the Coanda induced force by the propeller flow within the channel (in fact, the local 'apparent' C_μ^F of the flow that the actuation jets interact with is lower with increased local cross flow speed). Furthermore, unlike $C_T = 0$, the incremental increase by the addition of the WTE actuation appears to be similar to that of the CTE actuation alone and as the cross flow speed increases the fraction of overall drag owing to actuation drag decreases.

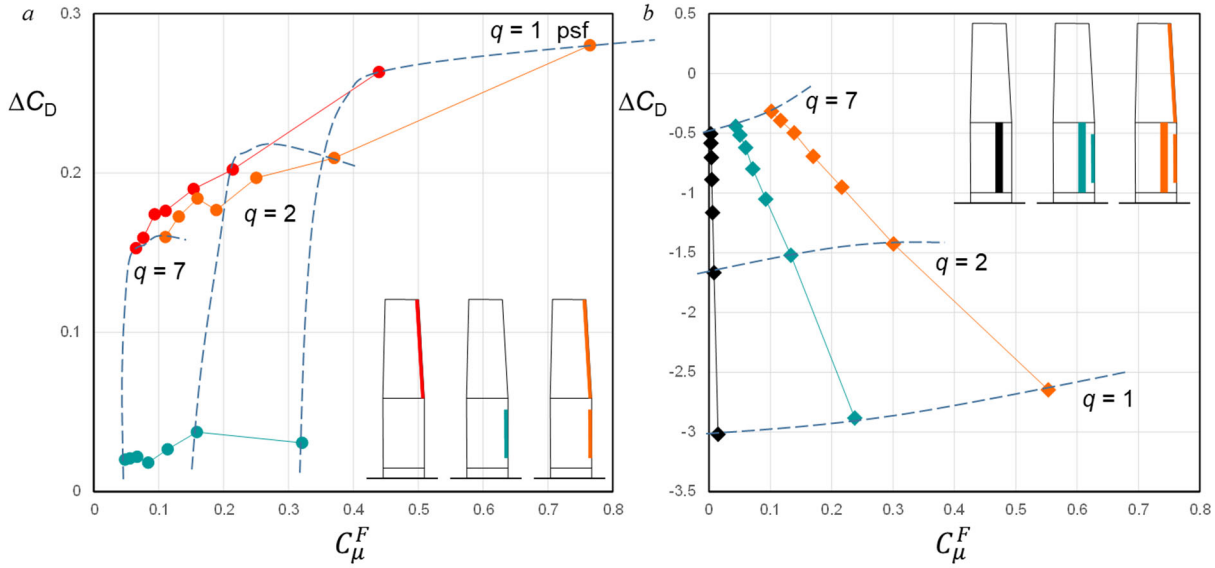

Figure 9. *As in Figure 8 for the drag increments relative to the baseline.*

The effects of fluidic actuation on the aerodynamic performance of the channel wing (with $C_T = 0$ and $C_T > 0$) are investigated within two regimes of angles of attack when the flow in the presence of trailing edge fluidic actuation is fully attached and a regime within which incipient stall can appear owing to actuation-effected changes in the pressure field over the suction surface even at

nominally at pre-stall angles of attack (cf. Vukasinovic et al., 2023b). While the flow induced by the propeller can bypass incipient separation within the channel, the effectiveness of the trailing edge actuation on the outboard section of the wing can be curtailed by partial separation over the main body of the wing. Therefore, within this range ($\alpha > 6^o$) circulation control is extended by leading-edge actuation (cf. Figure 1).

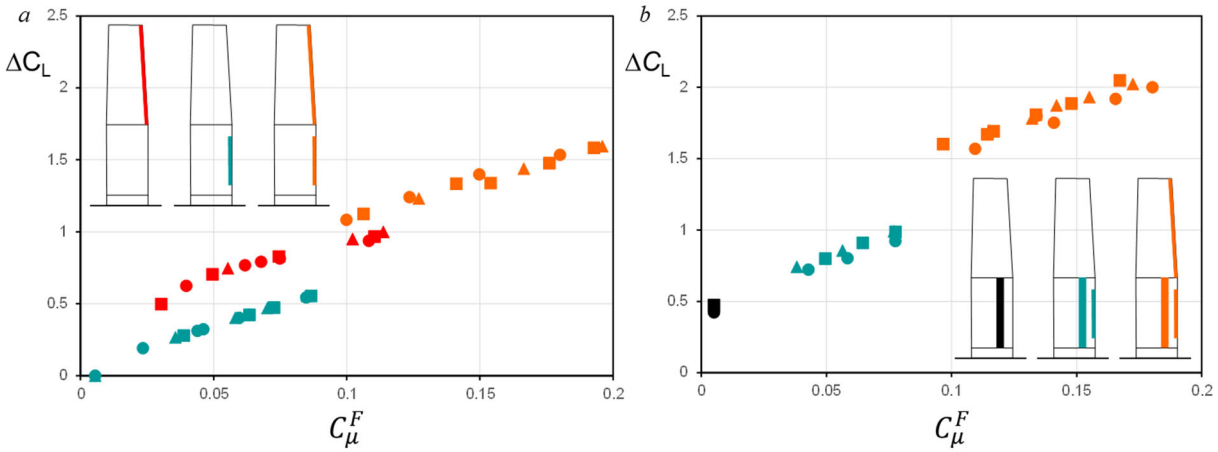

Figure 10. *The variation with C_μ^F of the lift increments relative to the baseline for actuation configurations CTE, WTE, and C/WTE at α = 0° (●), 2° (■), and 4° (▲), U_o = 18.2 m/sec (q = 4 psf) and C_T = 0 (a) and 0.6 (b).*

The effectiveness of the actuation for configurations CTE, WTE, and C/WTE in terms of the lift and drag increments relative to the baseline when the flow in the presence of actuation is fully attached (α = 0°, 2°, and 4°) at U_o = 18.2 m/sec (q = 4 psf) is demonstrated in Figures 10a and b, respectively for C_T = 0 (a) and 0.6 (b). It is remarkable that the lift increments induced by the actuation at C_T = 0 (Figure 10a) by each configuration vary nearly linearly with C_μ^F (except perhaps at the lowest C_μ^F) with the same rate of increase at all angles of attack, and that, in fact, all configurations exhibit nearly the same rate of increase of ΔC_L with C_μ^F despite the presence of the flap at ϕ = 45°. As noted in connection with Figure 8a, actuation with configurations CTE, WTE can be superposed at the same levels of total C_μ^F and this is reflected in the identical rate of change of ΔC_L with C_μ^F for C/WTE. These data also show that lift increments exceeding ΔC_L = 1.5 can be realized $C_\mu^F \approx$ 0.2. When the propeller is powered at C_T = 0.6 (Figure 10b), the effected lift increments in Figure 10a (C_T = 0) are simply offset by the additional lift induced by the propeller flow (just under ΔC_L = 0.5) flow as the lift increments induced by the propeller in the absence of fluidic actuation are nearly independent of α. Considering the lift offset effected by the propeller, lift increment of ΔC_L = 1.5 + 0.5 = 2 can be attained at lower $C_\mu^F \approx$ 0.18 compared to Figure 10a. Similar to Figure 10, the corresponding actuation effects on the lift-induced drag increments are presented in Figure 11a and b C_T = 0 and 0.6, respectively. As noted in connection with Figure 9a the lift induced drag by the CTE configuration is negligible. Furthermore, while for configurations WTE and C/WTE the drag increases with α, it appears to saturate and become nearly invariant with C_μ^F at higher actuation levels (as noted by the dashed line in Figure 12a), ΔC_L does not exhibit such saturation. This is consistent with the earlier findings of Vukasinovic et al. (2023a). An important consequence of this effect is that $\Delta C_L/\Delta C_D$ increases with C_μ^F. The saturation of the lift induced drag at C_T = 0 disappears (at least within this range) at C_T = 0.6 (Figure 12b) and exhibits monotonic rise with C_μ^F.

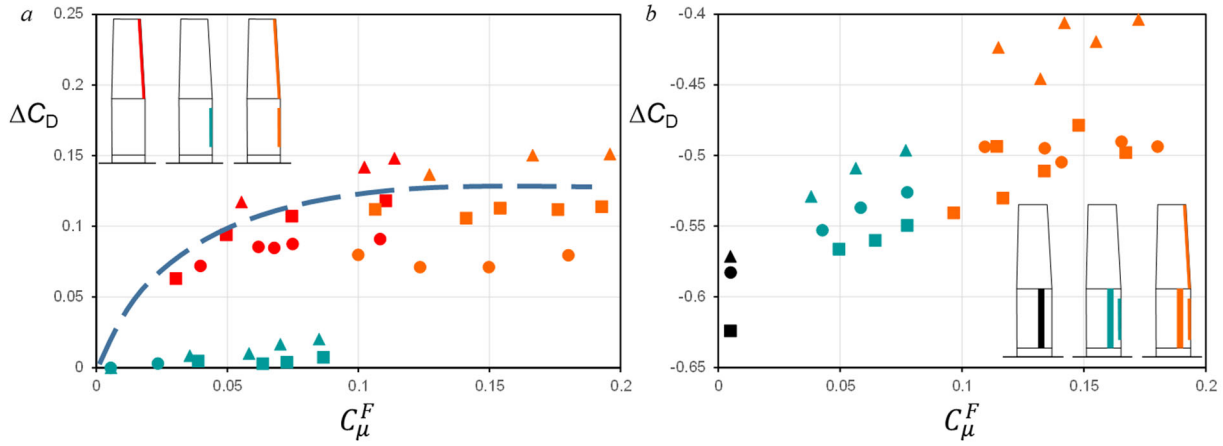

Figure 11. *As in Figure 10 for the drag increments relative to the baseline.*

Similar to the discussion in connection with Figures 10 and 11, the effectiveness of the actuation for configurations CTE, WTE, and C/WTE was also investigated within a range of α centered about the stall onset of the baseline wing α = 6°, 8°, and 10° (cf. Figure 4) as shown in Figures 12 and 13 for the lift and drag increments, respectively with C_T = 0 (a) and 0.6 (b). Figure 12a shows that the variation of the lift increments with C_μ^F becomes somewhat more complex with the onset of stall. While at α = 6° the flow is still fully attached, the variation of ΔC_L with C_μ^F is similar to α = 4° (Figure 10a). However, at α = 8° and 10°, there is precipitous drop in trailing edge actuation effectiveness. For example, for the same C_μ^F, ΔC_L with WTE actuation at α = 8° is only about half its level at α = 6°. In fact, tufts visualization near the wing's leading edge (not shown) indicated that while in the absence of actuation the baseline flow is nearly fully attached, at α = 8° actuation at the trailing edge can trigger leading edge separation that impedes the effectiveness of the actuation. As shown in Figure 12a, when actuation is activated along the leading edge of the outboard wing segment (WLE configuration), the trend of the lift increment becomes similar to the trend at α = 6° increasing the peak increment to about the same level as at lower α of $\Delta C_L \approx 1.5$

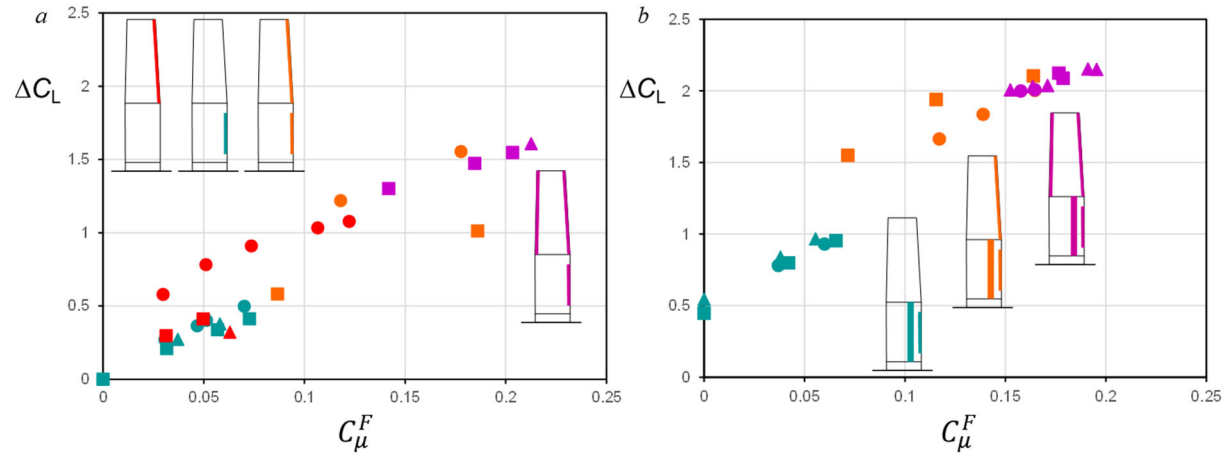

Figure 12. *The variation with C_μ^F of the lift increments relative to the baseline for actuation configurations CTE, WTE, C/WTE, and WLE at α = 6°(●), 8°(■), and 10°(▲), U_o = 18.2 m/sec (q = 4 psf) and C_T = 0 (a) and 0.6 (b).*

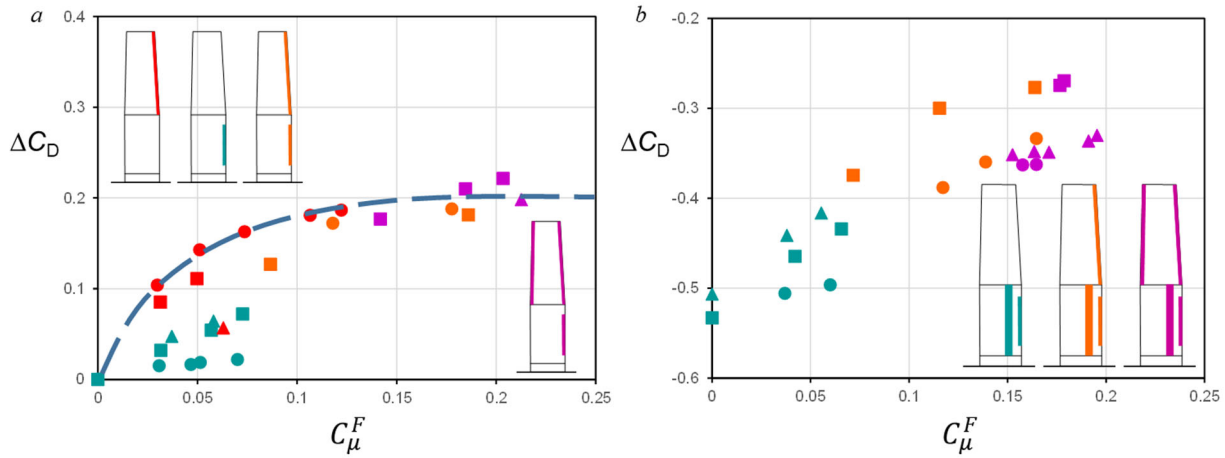

Figure 13. *As in Figure 12 for the drag increments relative to the baseline.*

while accounting for the total level of C_μ^F. Similar to $\alpha \leq 4°$, When the propeller is activated at $C_T = 0.6$ (Figure 12b), it adds a lift increment $\Delta C_L = 0.5$ and the effects of the incipient stall at $\alpha = 8°$ are somewhat mitigated. The addition of leading-edge actuation enables lift increments that are somewhat higher than 2. The corresponding effects on the drag increment at $\alpha = 6°$, 8°, and 10° are shown in Figure 13. These data show that the drag increment effected by the CTE and WTE configurations at $C_T = 0$ are larger than at the lower angles of attack indicating the streamwise tilt of the Coanda forces, but the data show the same trend of saturation at high C_μ^F including the effects of leading-edge actuation albeit at a higher level than in Figure 12a ($\Delta C_D \approx 0.2$ compared to 0.13). The effects in the presence of the powered propeller (Figure 13b) are commensurate with the effects on the lift increments in Figure 12b. Overall, the data in Figures 13 and 14 indicate that at least within this range of α, it is possible to maintain the same levels of aerodynamic effectiveness by using leading-edge actuation without a significant impact on the total C_μ^F.

The present findings are summarized in Figures 14a and b. At each angle of attack and $C_T = 0$, 0.6, and 1 the largest lift increment attained relative to the baseline was selected regardless of the

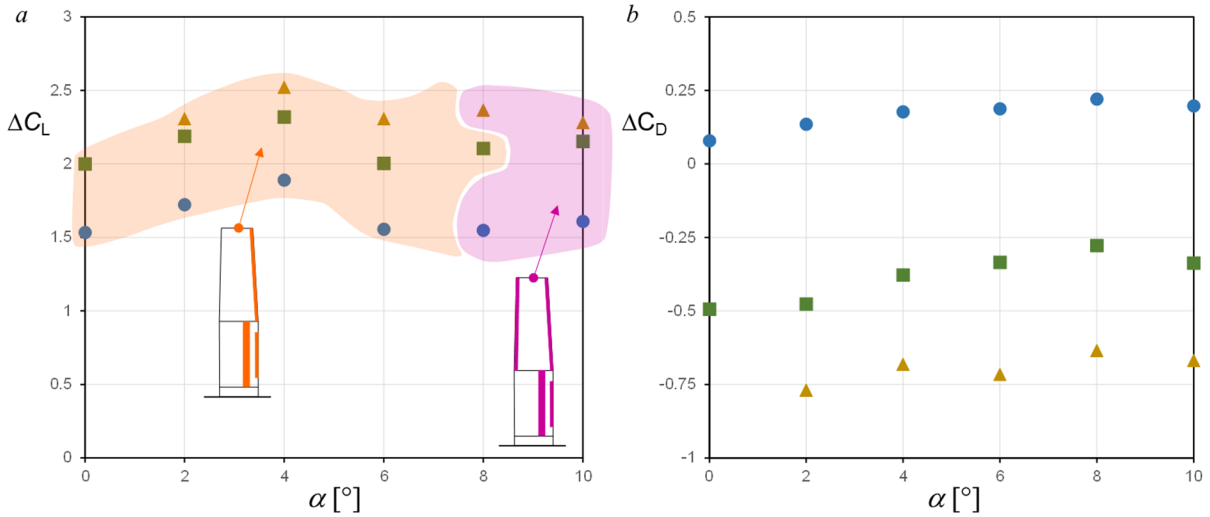

Figure 14. *a) Largest lift increments relative to the baseline at each angle of attack regardless of the actuation configuration and C_μ^F at $C_T = 0$ (●), 0.6 (■), and 1 (▲); and b) The corresponding drag increments (q = 4 psf).*

specific actuation configuration and C_μ^F. Figure 14a separates by highlighted background between combinations of CTE and WTE configurations at angles of attack up to incipient stall and combinations of CTE, WTE, and WLE configurations at higher α thereafter. These results exhibit reasonably uniform actuation effectiveness across the present range of α that yields $\Delta C_L \geq 1.5$ at $C_T = 0$ with a peak of $\Delta C_L \approx 1.8$ centered about $\alpha = 4°$. When the propeller is powered it leads to an additive increase in $\Delta C_L \approx 0.5$-0.6 at $C_T = 0.6$. Although at $C_T = 1$, the additional gain in lift increment is somewhat lower ($\Delta C_L \approx 0.7$ at $\alpha = 4°$), the highest attained increase in lift is $\Delta C_L = 2.5$ for $\alpha = 4°$. The corresponding increases in the lift induced drag are shown in Figure 14b. These data show a monotonic increase below and a peak at $\alpha = 8°$, with a significantly diminished rate of increase with α for $C_T = 0$ indicating general saturation as stall appears.

V. System Assessment of the Powered Channel Wing

The performance of the powered channel wing was assessed using a demonstrator UAV STOL transport configuration in the 5,000 lb class with a conventional high wing layout having the same wing aspect ratio (10) and a proportionally sized channel as the wind tunnel model and scaled up to 211 ft^2. The propulsive configuration was a hybrid electric with a turboprop providing power to the two engines in the wing. The vehicle configuration and propulsive layout are shown in Figure 15. The vehicle is powered by a Rolls-Royce Allision Model 250 C30 gas turbine engine

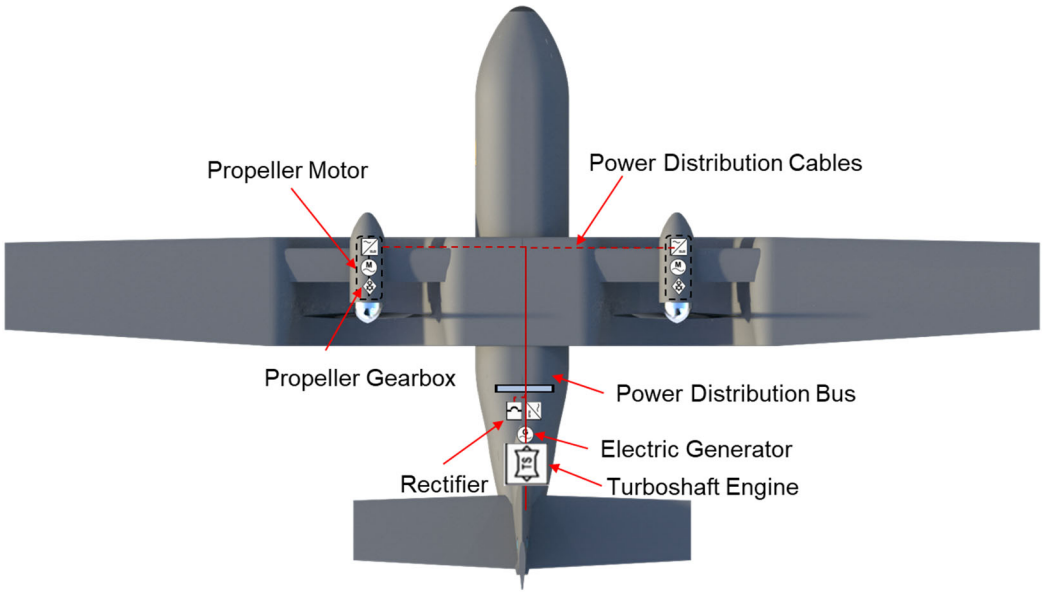

Figure 15. *UAV STOL transport configuration with a conventional high wing and propulsive layout.*

rated at 650 hp located in the aft fuselage. The engine cycle was modeled in Numerical Propulsion System Synthesis (NPSS) and calibrated to publicly available manufacturer information. The propeller diameter was selected based on the scaled channel of the wind tunnel test model with the blade geometry designed in XROTOR. Based on the gas turbine power available and an estimated cruise condition the propellers have five blades compared to three blades in the wind tunnel model. The electric motors were based on Siemens SP200D motors with the generator modeled at a constant efficiency. Actuation mass flow for CC was provided using three light weight Hamilton-Sundstrand T-62T-47C3P APUs that can provide 10 lbm/s air flow (pressure tanks and electric pumps were also considered).

Over 450 data points were gathered from the wind tunnel data in the absence and presence of propeller power. These data were used to generate second order polynomial surrogate models of the lift and drag coefficient as a function of angle of attack, C_μ^F of the actuator arrays and the thrust coefficient of the propeller. The surrogate models were reasonably accurate with R^2 values of 0.97-0.98 despite the data not being specifically tailored for surrogate modeling. These surrogates were used to estimate the lift and drag of the wing for the full-scale system where only the fuselage and tail drag were estimated and added to the drag coefficient assuming that their contributions to lift were negligible. The wind tunnel surrogate sensitivities of the lift to each input variable with all others held fixed are shown in Figure 16 with ranges based on the wind tunnel data with (blue) bands that show the 95% confidence interval based on the surrogates. These values are set based on final mass flow limited inputs optimized for maximum lift coefficient at takeoff.

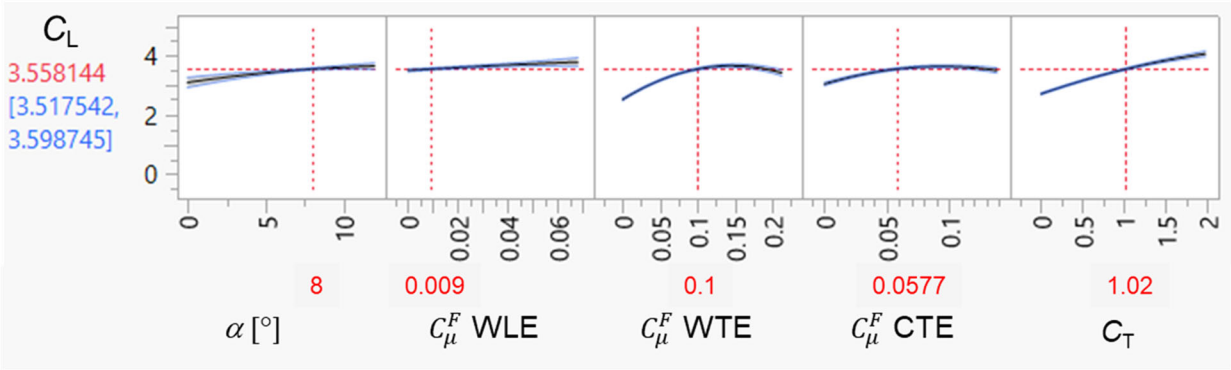

Figure 16. *Wind tunnel surrogate sensitivities of the lift to α, C_μ^F of actuation configurations WLE, WTE, CTE, and C_T. The ranges are based on the wind tunnel data and the blue band on each curve shows the 95% confidence interval based on the surrogates. These values are set based on final mass flow limited inputs optimized for maximum lift coefficient at takeoff.*

The CC mass flow for the full vehicle was estimated based on the wind tunnel data using the variation of effected C_μ^F with C_q for each of actuator array configurations. This relationship is shown in Figure 17 for the trailing edge actuation on the wing's outboard segment. The mass flow for the full vehicle was estimated by scaling the coefficients and the available mass flow was be allocated to each actuator bank based on the flight condition in order to optimize the attained lift coefficient in takeoff and landing. The aerodynamic and propulsive models were integrated into a takeoff and landing performance model in NASA's FLight OPtimization System (FLOPS) aircraft sizing and performance modeling tool. The detailed takeoff and landing module in FLOPS estimates the liftoff distance,

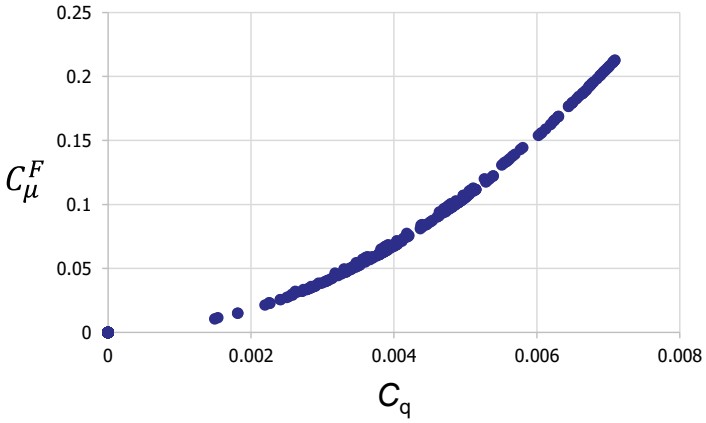

Figure 17. *Variation of the momentum coefficient of wing outboard trailing edge actuation WTE with actuation mass flow rate coefficient.*

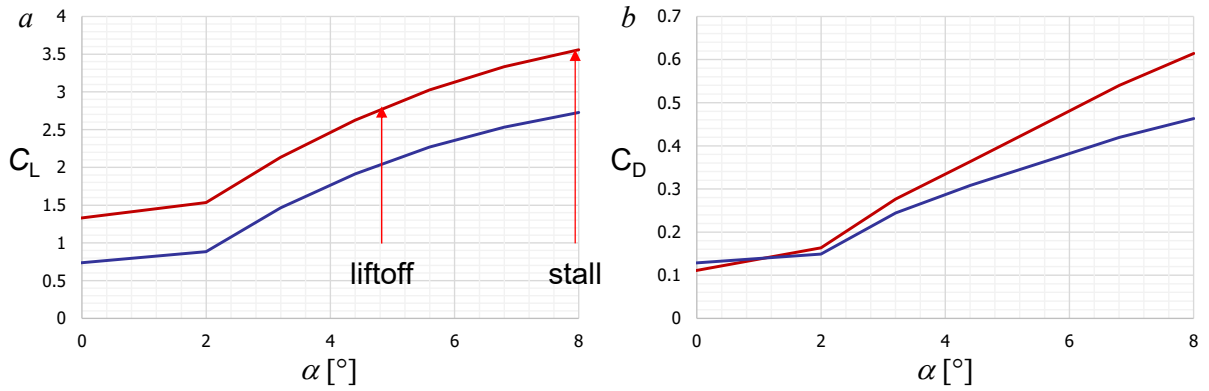

Figure 18. *The variation with a of the highest lift (a) and corresponding drag (b) during **takeoff** and **landing** at the actuation mass flow limits enforced during the wind tunnel tests. The takeoff rotation and stall conditions at takeoff are marked.*

clearance over obstacle distance, and the landing distance through a series of trajectory simulations.

A challenge posed by using fluidic circulation control compared to conventional flap systems is the added degree of freedom of actuation mass flow rate in addition to the angle of attack. The FLOPS takeoff and landing module is not designed to model this additional degree of freedom and was therefore modified to link the level of CC actuation to the angle of attack during takeoff rotation. The trajectory simulation selects the actuation level necessary at each stage of the takeoff and landing based on the actual lift required rather than employing the maximum available actuation for maximum lift that would unnecessarily increase induced drag during ground roll. No actuation is used while sitting on the ground and during the initial part of the takeoff ground roll, and the takeoff rotation results in increased actuation mass flow rate. The maximum lift coefficient was estimated by optimizing the mass flow distribution across the actuator arrays to achieve the highest lift at the mass flow limits that were enforced during the wind tunnel tests based on the available APU specification and the mass flow was linearly scaled down to zero at $\alpha = 2^o$. The variation with α of each of the resulting lift and drag is shown in Figures 18a and b, respectively on which the

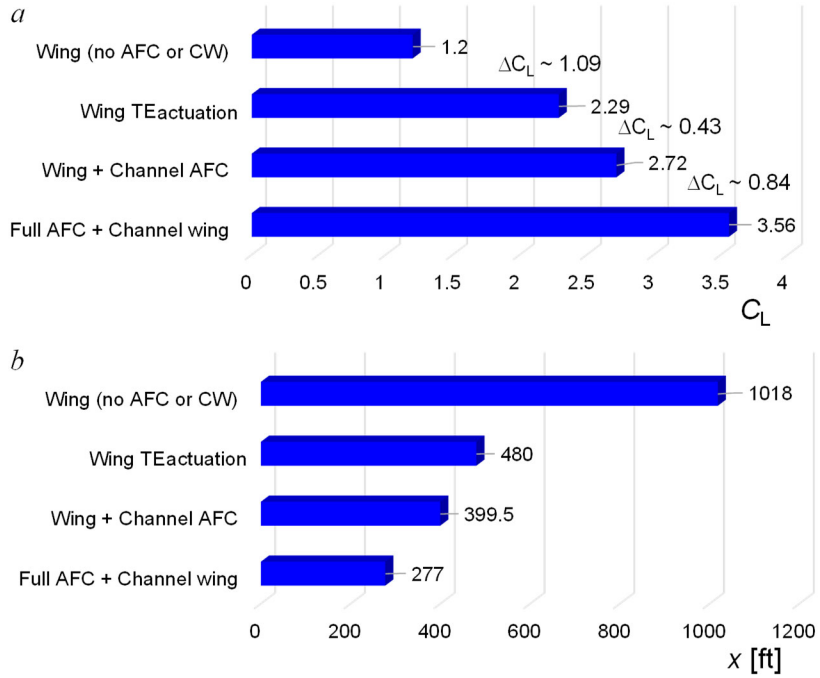

Figure 19. *The relative contributions of the channel wing effect from the propellers and the two banks of fluidic actuators at the mass flow limit available from the APU on: a) The maximum lift coefficient for liftoff, and b) The resulting liftoff distance in feet.*

takeoff rotation and stall conditions at takeoff are marked. It should be noted that the landing configuration has substantially less lift and drag since the propulsive effect of the channel wing is significantly reduced due to a lower thrust coefficient in descent and landing. The relative contributions of the channel wing effect from the propellers and the two banks of fluidic actuators on the maximum lift coefficient for liftoff is shown in Figure 19a along with the resulting liftoff distance for each in Figure 19b. This includes the mass flow limit available from the APU. The two banks of fluidic actuators combined provide the largest ΔC_L with a substantial contribution from the channel wing.

These investigations show that the liftoff distance for takeoff of the vehicle is reduced by about 73%. The liftoff speed is about 52 knots and the total takeoff field length over a 50 ft obstacle is 604 ft at sea-level, with an estimated landing distance of 667 ft. These findings demonstrate the potential of fluidic based aerodynamic flow control to enable substantial takeoff and landing performance improvements of channel wing configurations while considering realistic limits on the available actuation mass flow.

VI. Conclusions

Enhanced aerodynamic performance of a channel wing model using fluidic based circulation control (CC) for improved short takeoff and landing (STOL) by reducing the takeoff speed and/or distance was assessed in low-speed wind tunnel investigations that were and used for system assessment UAV STOL transport configuration. Circulation control was implemented by exploiting the Coanda effect of integrated arrays of fluidically-oscillating wall jet actuators along the trailing edges of both the channel (along a rounded trailing edge) and the outboard wing segment (merged onto a flap deflected at 45°). While these investigations focused primarily on pre-stall angles of attack, the effects of circulation control were also extended into the onset of stall by an additional array of wall jets along the leading edge of the outboard wing section.

The aerodynamic effects of circulation control measured by lift and lift induced drag increments were assessed in the absence and presence of power to the channel propeller at varying levels of the thrust when powered. Following benchtop development and characterization of actuators arrays over the trailing edges of the outboard wing segment and channel, the jet arrays were integrated into the wind tunnel model and characterized *in situ*, in the absence of cross flow, yielding the aerodynamic loads effected by the actuation on the model that was used to determine the actuation momentum coefficient C_μ^F. It was shown that the aerodynamic loads effected by the individual actuator arrays on the wing's outboard segment and the channel are additive in either the absence and presence of propeller power. Moreover, the control-induced lift increment ΔC_L depended only on the aggregate C_μ^F that is split between the trailing edge actuation arrays. As a result, the actuation can be spread between the actuator arrays as may be needed for aerodynamic maneuvering and potentially simplifying the fluidic system.

At low angles of attack $0° \le \alpha \le 4°$, CC induced an increase is the lift coefficient up to $\Delta C_L = 1.5$, while the propeller powered at $C_T = 0.6$ contributed additional $\Delta C_L = 0.5$ over the channel for $\Delta C_L = 2$. When CC control is extended into incipient stall at $6° \le \alpha \le 10°$, the control effectiveness drops (to nearly half the level at low angles of attack) at $\alpha > 8°$ due to the onset of the leading-edge separation. However, it was possible to recover nearly the same overall ΔC_L (2) once some of the total C_μ^F was diverted to the leading-edge actuators for flow reattachment. Overall, a rather consistent

aerodynamic performance in the absence and presence of propeller power was achieved over the full range of $0° \leq \alpha \leq 10°$ with peaks of $\Delta C_L = 2.3$ and 2.5, for $C_T = 0.6$ and 1, respectively, at $\alpha = 4°$.

The wind tunnel data was integrated into a system level assessment model for a hybrid electric STOL transport UAV. The model included estimates of actuation mass flow source and enforced realistic limits on the aerodynamics with this system level constraint. It was shown that circulation control can enable up to 73% reduction in the liftoff distance, demonstrating its potential for integration into realistic channel wing platform configurations.

Acknowledgment

This research was developed with funding from the Defense Advanced Research Projects Agency (DARPA) Control of Revolutionary Aircraft with Novel Effectors (CRANE) Program. The views, opinions and/or findings expressed are those of the authors and should not be interpreted as representing the official views or policies of the Department of Defense or the U.S. Government.

The authors acknowledge GTRI Principal Research Engineer Burt Jennings and GT Research Engineer Dr. Svyatoslav Yorish for their assistance in the wind tunnel testing, particularly with respect to the wind tunnel model and auxiliary hardware design, assembly, shakedown, and operation.

References

Blick, E. F. and Homer, V., "Power-on Channel Wing Aerodynamics," *Journal of Aircraft*, Vol. **8** (4), pp. 234-238, 1971.

Custer, W., R., *Aeroplane*, US Patent #1,708,720, 1929.

Davidson, I. M., "The Jet Flap," *The Aeronautical Journal*, Vol. **60** (541), pp.25-50, 1956.

Dimmock, N. A., "An Experimental Introduction to the Jet Flap," Aeronautical Research Council Technical Report C.P. No. 344, 1957.

Englar, R. and Campbell, B., "Development of Pneumatic Channel Wing Powered-Lift Advanced Super-STOL Aircraft," *AIAA Paper* 2002-2939, 2002.

Gunther, C., Marchman, J. and VanBlarcom, R., "Comparison of Channel Wing Theoretical and Experimental Performance," *AIAA Paper* 2000-0257, 2000.

Haus, F., "The Use of Slots for Increasing the Lift of Airplane Wings," NACA-TM-635, 1931.

Jones, G. S., "Pneumatic flap performance for a 2d circulation control airfoil, steady and pulsed," *Proceedings of the 2004 NASA/ONR Circulation Control Workshop, Part 2*, 2005.

Keane, P.M. and Keane, A.J., "Use of Custer Channel Wings – Wing Ducts on Small UAVs," *Journal of Aerospace Engineering*, **29** (3), 04015059, 2016.

Mihalik, J. and Keane, A.J., "Custer Channel Wings for Short Takeoff and Landing of Unmanned Aircraft," *Journal of Aircraft*, **59** (1), pp.196-205, 2022.

Pasamanick, J., "Langley Full-Scale-Tunnel Tests of the Custer Channel Wing Airplane," *NACA-RM-L53A09*, 1953.

Radespiel, R., Burnazzi, M., Casper, M., and Scholz, P., "Active flow control for high lift with steady blowing," *The Aeronautical Journal*, Vol. **120** (1223), pp.171-200, 2016.

Vukasinovic, B., Glezer, A., and Funk, R.B., "DARPA CRANE Circulation Control using Arrays of Discrete Fluidic Actuator Jets," *AIAA Paper* 2023-1992, 2023a.

Vukasinovic, B., DeSalvo, M., Funk, R.B., and Glezer, A., "Aerodynamic Flow Control of a Channel Wing," *AIAA Paper* 2023-4348, 2023b.

Williams, J., Butler, S.F.J. and Wood, M.N., "The Aerodynamics of Jet Flaps," *Aeronautical Research Council*, R&M No. 3304, 1961.